Merged Cloud and Precipitation Dataset from the HIAPER GV for the Cloud System Evolution in the Trades (CSET) Campaign

M. CHRISTIAN SCHWARTZ,[a] VIRENDRA P. GHATE,[a] BRUCE. A. ALBRECHT,[b] PAQUITA ZUIDEMA,[b]
MARIA P. CADEDDU,[a] JOTHIRAM VIVEKANANDAN,[c] SCOTT M. ELLIS,[c] PEI TSAI,[c]
EDWIN W. ELORANTA,[d] JOHANNES MOHRMANN,[e] ROBERT WOOD,[e] AND
CHRISTOPHER S. BRETHERTON[e]

[a] *Argonne National Laboratory, Lemont, Illinois*
[b] *University of Miami, Miami, Florida*
[c] *Earth Observing Laboratory, NCAR, Boulder, Colorado*
[d] *University of Wisconsin–Madison, Madison, Wisconsin*
[e] *University of Washington, Seattle, Washington*

ABSTRACT

The Cloud System Evolution in the Trades (CSET) aircraft campaign was conducted in the summer of 2015 in the northeast Pacific to observe the transition from stratocumulus to cumulus cloud regime. Fourteen transects were made between Sacramento, California, and Kona, Hawaii, using the NCAR's High-Performance Instrumented Airborne Platform for Environmental Research (HIAPER) Gulfstream V (GV) aircraft. The HIAPER W-band Doppler cloud radar (HCR) and the high-spectral-resolution lidar (HSRL), in their first deployment together on board the GV, provided crucial cloud and precipitation observations. The HCR recorded the raw in-phase (I) and quadrature (Q) components of the digitized signal, from which the Doppler spectra and its first three moments were calculated. HCR/HSRL data were merged to develop a hydrometeor mask on a uniform georeferenced grid of 2-Hz temporal and 20-m vertical resolutions. The hydrometeors are classified as cloud or precipitation using a simple fuzzy logic technique based on the HCR mean Doppler velocity, HSRL backscatter, and the ratio of HCR reflectivity to HSRL backscatter. This is primarily applied during zenith-pointing conditions under which the lidar can detect the cloud base and the radar is more sensitive to clouds. The microphysical properties of below-cloud drizzle and optically thin clouds were retrieved using the HCR reflectivity, HSRL backscatter, and the HCR Doppler spectrum width after it is corrected for the aircraft speed. These indicate that as the boundary layers deepen and cloud-top heights increase toward the equator, both the cloud and rain fractions decrease.

1. Introduction

A physically reasonable treatment of low clouds within climate models is required for the realistic modeling of the climate's sensitivity to greenhouse gas forcing (e.g., Wetherald and Manabe 1988; Tiedtke 1993; Stephens 2005). Furthermore, low clouds account for a great deal of intermodel variability in cloud feedback factors (Bony and Dufresne 2005; Zhang et al. 2013). One persistent difficulty with modeling marine boundary layer (MBL) clouds is accurately capturing the transition of widespread decks of stratocumulus clouds through a regime of cumulus below the stratocumulus clouds and finally into a deeper cumulus cloud regime (Wood and Bretherton 2004; Sandu et al. 2010). This transition occurs as offshore stratocumulus decks are advected by the trade winds to warmer sea surface temperatures (SSTs), deepening and weakening the boundary layer inversion. Several mechanisms behind this transition have been proposed, the dominant mechanism being a warming and deepening of the marine boundary layer, in which turbulence entrains free-tropospheric air through the MBL's top (Bretherton and Wyant 1997; Sandu and Stevens 2011).

Corresponding author: Virendra P. Ghate, vghate@anl.gov

Other proposed mechanisms that influence the characteristics of the transition, as opposed to the occurrence of the transition itself, include the precipitation flux within the MBL, changes in the large-scale subsidence, diurnal variations in the warming of the MBL clouds, changes in the water vapor above the MBL, and changes in aerosol concentrations (Wang et al. 1993; Sandu et al. 2010; Yamaguchi et al. 2017; Abel et al. 2017).

The Cloud System Evolution in the Trades (CSET) field campaign was conducted during July and August 2015 (Albrecht et al. 2019) with the goal of improving the process-level understanding of the transition from stratocumulus to cumulus cloud regime in the North Pacific. During CSET, the High-Performance Instrumented Airborne Platform for Environmental Research (HIAPER) Gulfstream V (GV) aircraft, owned and operated by the National Science Foundation (NSF) and the National Center for Atmospheric Research (NCAR; Laursen et al. 2006), was used to make detailed measurements of aerosol, cloud, precipitation, and thermodynamic properties. The HIAPER made a total of 16 research flights (RFs) during CSET, 14 of which were transects between Sacramento, California, and Kona, Hawaii. On the outbound flight from Sacramento to Kona, detailed low-level sampling was made in 3–4 locations in the stratocumulus region. Using the Hybrid Single-Particle Lagrangian Integrated Trajectory model (HYSPLIT; Stein et al. 2015), the locations of the sampled air masses 2 days later were calculated. The inbound flights from Kona to Sacramento were made 2 days later, and during them, detailed low-level sampling was conducted at the HYSPLIT model project locations of the air masses sampled earlier. This allowed sampling of the air masses in a quasi-Lagrangian fashion as compared to the more traditional Eulerian sampling thereby capturing the evolution of the cloud field. During CSET, detailed low-level sampling was made in 27 locations on the outbound flight and 36 locations on the inbound flights. The detailed sampling at the low levels typically included the following four ~10-min-long legs: 1) a near-surface leg [100–140 m above mean sea level (MSL)], 2) an in-cloud leg, 3) a porpoise leg during which the GV went ~100 m above and below the boundary layer inversion, and 4) an above-cloud leg. The low-level sampling locations were labeled alphabetically as they were made for each flight (e.g., RF02-A and RF02-B for first and second low-level sampling modules during RF02). Depending on the boundary layer divergence and wind fields, at times, two or more low-level sampled locations corresponded to the same air mass as revealed by the HYSPLIT trajectory analysis, and hence during CSET, a total of 18 air masses were sampled twice in a quasi-Lagrangian fashion. Further details on the sampling strategies and the mean conditions observed during CSET can be found within Albrecht et al. (2019), Mohrmann et al. (2019, manuscript submitted to *Mon. Wea. Rev.*), and Bretherton et al. (2019).

A notable feature of the CSET campaign was the first deployment of the HIAPER W-band Doppler cloud radar (HCR), together with the high-spectral-resolution lidar (HSRL). These systems were included on the CSET GV deployment to remotely sense cloud and precipitation. A cloud and precipitation data product that includes cloud macro- and microphysical properties, derived from multiple instruments on a georeferenced grid, is essential for performing cloud-related studies. Previous studies have documented algorithms using surface-based radar and lidar data (Clothiaux et al. 2000; Illingworth et al. 2007; Feng et al. 2014) and aircraft radar, lidar, and in situ data (e.g., Klingebiel et al. 2015; McGill et al. 2004; Wang et al. 2009, 2012). The CSET campaign was the first deployment of the HCR and HSRL upon the NCAR GV plane. This aircraft was designed for long, high-altitude flying at higher speeds than those of planes typically used for boundary layer research. As such, it is important to establish how well the HCR and HSRL datasets can be applied to retrieve microphysical parameters of shallow clouds from a platform that is faster moving than those used in previous aircraft studies. In this article, we present the gridded cloud and precipitation data derived by merging the data collected by HCR and HSRL for the CSET campaign. Results from two separate datasets are shown: one from a more sophisticated retrieval relying on three inputs to discriminate cloud and precipitation parameters and another, simpler retrieval distinguishing cloud from precipitation using a radar reflectivity threshold, providing more statistics but less microphysical detail.

The operational settings of the HCR and the HSRL during CSET and the data are described in section 2, which is followed by a description the technique used to identify cloud boundaries and hydrometeor type (section 3). The techniques used to retrieve cloud and precipitation microphysical properties are described in section 4, and the article is concluded with a summary and future work in section 5.

2. Instrumentation and data

The HCR (Vivekanandan et al. 2015) and the HSRL (Eloranta 2005) were commissioned specifically for the HIAPER GV aircraft (Rauber et al. 2017). The HCR operates at a frequency of 95 GHz and can scan both along-track and cross-track directions. As attenuation by water vapor in a marine environment limited the HCR's sensitivity to observe nonprecipitating clouds in off-zenith angles, during CSET the HCR was mostly operated in

TABLE 1. Operational parameters of the HIAPER cloud radar and the file sizes of collected data.

Parameter	Specification
Central frequency	94.4 GHz
Antenna diameter	0.30 m
Antenna gain	46.21 dB
3-dB beamwidth	0.68°
Peak transmit power	1.6 kW
Pulse width	0.256 μs
Unambiguous range	15.2 km
Pulse repetition frequency	9.864 kHz
Range resolution	19.2 m
Dead zone	203 m
Sensitivity (0-dB SNR)	-39.6 dBZ at 1 km
Unambiguous Doppler velocity	± 7.75 m s^{-1}
Dwell time	100 ms
Polarization	Linear
30-s I and Q data (IWRF format)	1.8 GB
30-s I and Q data (netCDF)	1.1 GB
30-s Doppler spectra and moments (netCDF)	41 MB
I and Q data per flight (IWRF format)	$\sim$1.7 TB
I and Q data per flight (netCDF)	$\sim$1 TB
Doppler spectra and moments per flight (netCDF)	$\sim$36.4 GB
I and Q data for CSET (IWRF format)	26 TB
I and Q data for CSET (netCDF)	16 TB
Doppler spectra and moments for CSET (netCDF)	567 GB

TABLE 2. Operational parameters of the HSRL onboard the HIAPER during CSET.

Parameter	Specification
Wavelength	532 nm
Intrinsic range resolution	7.5 m
Range resolution used for CSET	20 m
Minimum temporal resolution	0.5 s
Field of view	0.025°
Average power	300 mW

either a zenith or nadir-pointing mode. The HCR recorded the time series of the in-phase (I) and quadrature (Q) components of the backscattered signal along with the first three moments of the Doppler spectrum calculated using the pulse-pair technique (Zrnic 1977). Codes were developed to process the I and Q data available in the Integrated Weather Radar Facility (IWRF) format into calculated Doppler spectra and their moments in the Network Common Data Form (netCDF), at desired resolutions, using the technique proposed by Clothiaux et al. (1996). The operational parameters of the HCR during CSET, and dataset sizes collected, are documented in Table 1. We note that the cloud radars that are part of the Atmospheric Radiation Measurement (ARM) program (Mather and Voyles 2013) operate at a similar pulse repetition frequency (PRF) of 10 KHz. As the focus of CSET was on warm boundary layer clouds that have spherical water drops, data in the cross-polarization channel were not used in this study. If used, the file sizes would be approximately double those reported in Table 1.

The HSRL is a visible-wavelength lidar (532 nm) with the ability to operate in zenith- or nadir-pointing mode (operational settings of the HSRL during CSET are shown in Table 2). To avoid specular reflection from the ocean surface, the HSRL was pointing 4° from the

fuselage while pointing down. The direction of the HSRL beam tilt was toward the left wing of the GV away from the HCR reflector pod that was mounted on the right wing. The HSRL recorded the calibrated backscatter at 2-Hz temporal and 7.5-m range resolutions. The extinction coefficient can also be calculated using the calibrated backscatter; however, because of high variability, the extinction can only be calculated by averaging for several ($\sim$5–10) seconds, which is too coarse for sampling small cumuli ($\sim$1 km) at the cruising speed of the GV (125–220 m s^{-1}). Hence, the HSRL extinction coefficients are not incorporated into the hydrometeor classification.

Suites of remotely sensed microphysical retrievals also commonly include liquid water path, which can serve as a geophysical constraint on the microphysical retrievals from active remote sensors (e.g., Frisch et al. 1995). The CSET campaign included an upward-looking millimeter-wave G-band microwave radiometer (GVR) for this purpose, operating at four double-sideband channels (± 1, ± 3, ± 7, and ± 14 GHz) off the center of the 183.3-GHz water vapor line (Pazmany 2007). GVR data had previously been applied successfully in a stratocumulus-focused aircraft campaign (Zuidema et al. 2012; Terai et al. 2012; Painemal and Zuidema 2013). However, the calibration of the GVR instrument was unsatisfactory during the CSET campaign. In particular, the brightness temperatures at the four frequencies were not consistent with each other and with radiative computations, with the frequency near the line center being too warm and the remaining three brightness temperatures being too cold or negative. Given the great sensitivity of the retrieval results to the instrument calibration, it was decided not to utilize the data from the GVR in this study.

The first three moments of the Doppler spectrum calculated using the pulse-pair technique are available through the NCAR CSET website at 10- and 100-Hz temporal resolutions. In this technique, mean Doppler velocity and Doppler spectrum width are estimated from autocorrelations of the sampled complex radar returns, whose real and imaginary parts are provided at the PRF as I and Q sample streams (Miller and
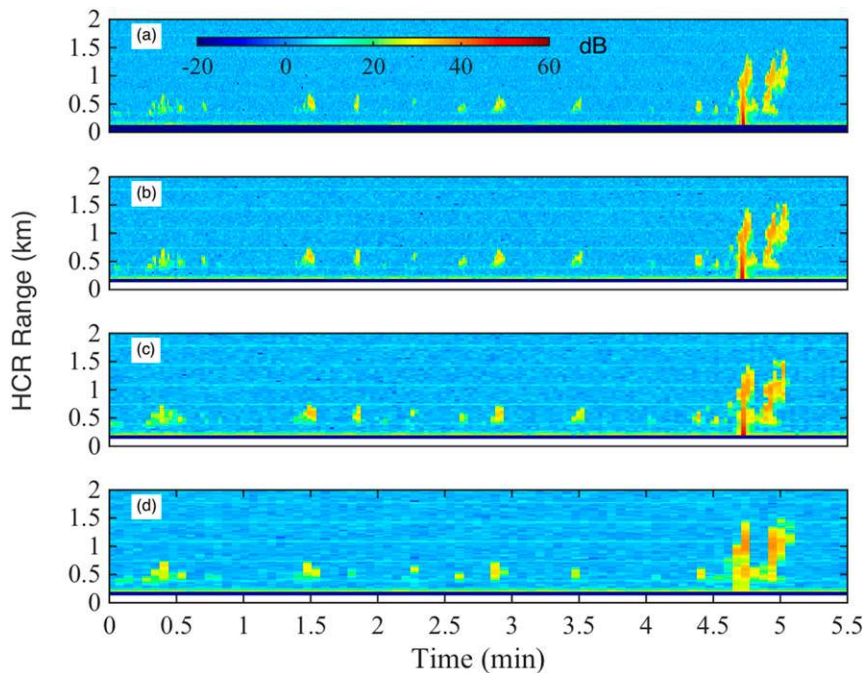
FIG. 1. Time–range profiles of the SNR calculated from the spectral processing at a resolution of (a) 2, (b) 1, (c) 0.65, and (d) 0.5 Hz starting at 1813:00 UTC 29 Jul 2015. The average aircraft speed during this segment was $123\,\mathrm{m\,s^{-1}}$, and the radar was flying at 100 m MSL.

Rochwarger 1972). The 100-Hz-resolution pulse-pair moments have a significant amount of noise because of a lower number of samples; thus, the 10-Hz pulse-pair moments were used. Ground-based stationary radars can calculate useful spectra at 1–2-s temporal resolution (Kollias et al. 2014). These calculations benefit from a cloud movement driven by boundary layer winds that are relatively low. In contrast, the nominal speed of the GV was $\sim220\,\mathrm{m\,s^{-1}}$ during ferry legs and $\sim130\,\mathrm{m\,s^{-1}}$ during the low-level sampling legs. As Doppler spectra are desirable for the ongoing research purposes, and there is considerable debate about the usefulness of the width of Doppler spectrum calculated from the pulse-pair technique for performing cloud and drizzle property retrievals (discussed later), Doppler spectra were computed by performing fast Fourier transforms (FFTs) of windowed versions of the aforementioned I and Q signal data streams. The moments of the Doppler spectra were computed from the Doppler spectra with the noise level in the spectra determined using the technique proposed by Hildebrand and Sekhon (1974). To test for an appropriate temporal resolution of the Doppler spectra for CSET, the Doppler spectra and their first three moments were calculated using 256 FFT points at 2-, 1-, 0.65-, and 0.5-Hz temporal resolutions (Fig. 1). These correspond to 20, 40, 80, and 160 spectral averages and 0.5-, 1-, 1.5-, and 2-s temporal resolutions,

respectively. A higher number of spectral averages yield smoother spectra but at the cost of a lower temporal resolution for the moments. This adversely affects the detection of cloud boundaries and thereby the determined echo fraction. For any temporal resolution coarser than 2 Hz (0.5 s), the HCR did not fully adequately resolve the shallow cumulus. For the cloud field shown in Fig. 1, the echo fraction (not shown) at the cumulus cloud base was 20% and 30% from moments calculated at 2 and 0.5 Hz, respectively. The higher cloud fraction at a coarser temporal resolution was due to lower number of total samples in the moments calculated at 0.5 Hz, which increased the number of cloudy samples by averaging in clear with cloudy volumes of air. The averaging of cloudy and clear volumes of air (beamfilling effect) also affects the microphysical retrieval techniques. Driven by these considerations, the spectra and moments are calculated at a 2-Hz resolution using 256 FFT points. With 256 FFT points, the resolution of the Doppler spectra is $6.05\,\mathrm{cm\,s^{-1}}$. A lower number of FFT points allows for a higher number of spectral averages but also decreases the resolution of the Doppler spectra, making it difficult to identify Mie notches (Kollias et al. 2002). The moments calculated from the Doppler spectra revealed a direct current (dc) signal (at $0\,\mathrm{m\,s^{-1}}$ velocity bin) that occur every 18 range gates. These are masked in the calculated moments.
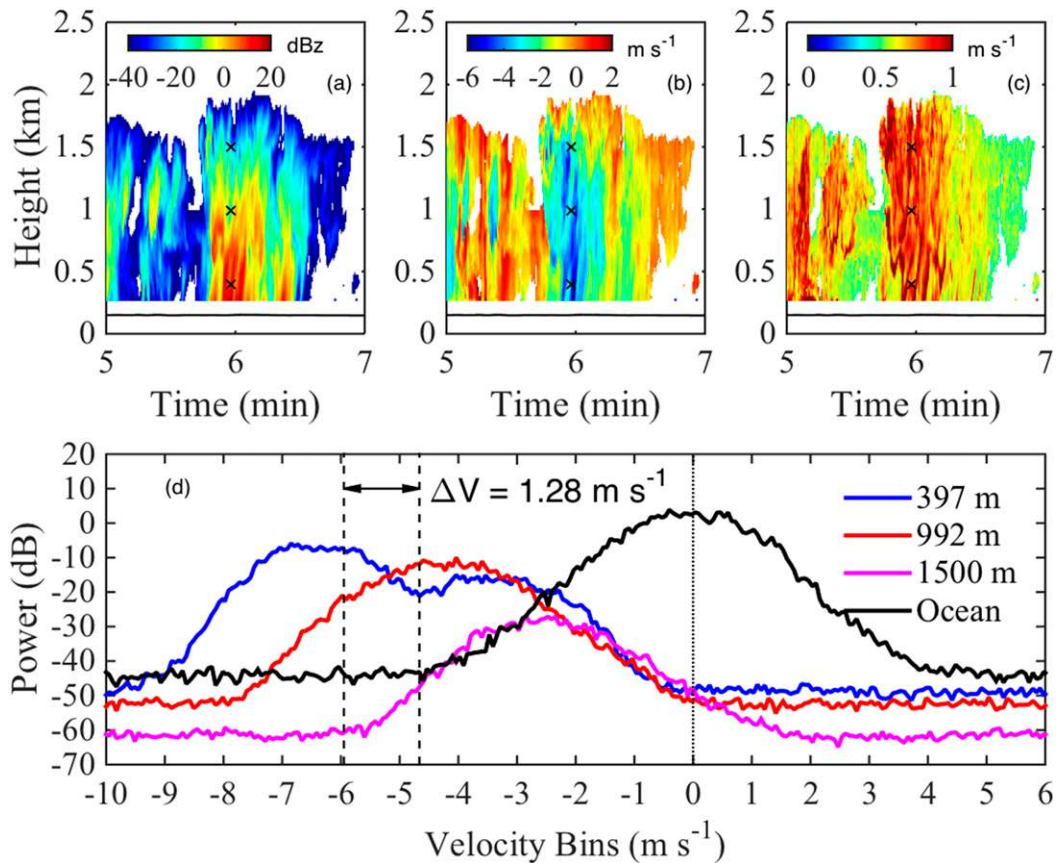
FIG. 2. Time–height profile of HCR (a) reflectivity, (b) mean Doppler velocity, and (c) spectrum width on 19 Jul 2015. The time period starts at 1935:58 UTC. The height is GV altitude (km MSL). (d) The Doppler spectra at the three levels marked by $\times$ in (a)–(c). The ocean spectra in (d) were recorded on the previous above-cloud leg. The theoretical and observed locations of the Mie notch are shown by vertical dashed lines, with the difference between them denoting vertical air motion. The spectra were dealiased before plotting. Negative velocities denote downward vertical motion.

The cause of this dc signal is still unknown and is being investigated further.

An example of the calculated Doppler spectra for a rain event observed on 19 July 2015 (RF07) is shown in Fig. 2. The GV was flying about 140 m above the surface and the HCR and HSRL were pointing upward. Heavy drizzle is evident through reflectivity values exceeding 10 dBZ, mean Doppler velocities less than $-4\,\mathrm{m\,s}^{-1}$, and a spectrum width greater than $1\,\mathrm{m\,s}^{-1}$. Doppler spectra from three levels during this period and from the ocean surface observed during nearby leg are shown in Fig. 2d. Because of the radar's finite beamwidth and the high speed of GV, the ocean spectra are broadened significantly (Sloss and Atlas 1968). Although broadened because of aircraft motion, the Mie notch is visible in the spectra collected at 397 m. The theoretical location of the Mie minimum at the W-band frequency is $5.95\,\mathrm{m\,s}^{-1}$. Hence, the difference between the location of the Mie minimum and $5.95\,\mathrm{m\,s}^{-1}$ corresponds to the vertical air motion (Kollias et al. 2002), which in this example is an updraft of $1.28\,\mathrm{m\,s}^{-1}$. A Mie notch was observed for several samples during this segment below 1 km, and currently, efforts are underway to objectively determine the Mie minimum to retrieve vertical air motion in drizzling periods for the entire campaign using the technique proposed by Giangrande et al. (2010) and Fang et al. (2017).

The HCR is calibrated internally (Vivekanandan et al. 2015) and using the ocean backscatter signal (Rilling et al. 2017). The reflectivity is calculated from the spectra-determined signal-to-noise ratio (SNR) using a calibration constant determined for the pulse-pair reflectivity. The probability density function (PDF) of HCR reflectivity, similar to the contoured frequency by altitude diagram (CFAD) proposed by Yuter and Houze (1995), observed during the entire CSET campaign as a function of the HCR range is shown in Fig. 3a. The two modes of samples below 4 km and between 4
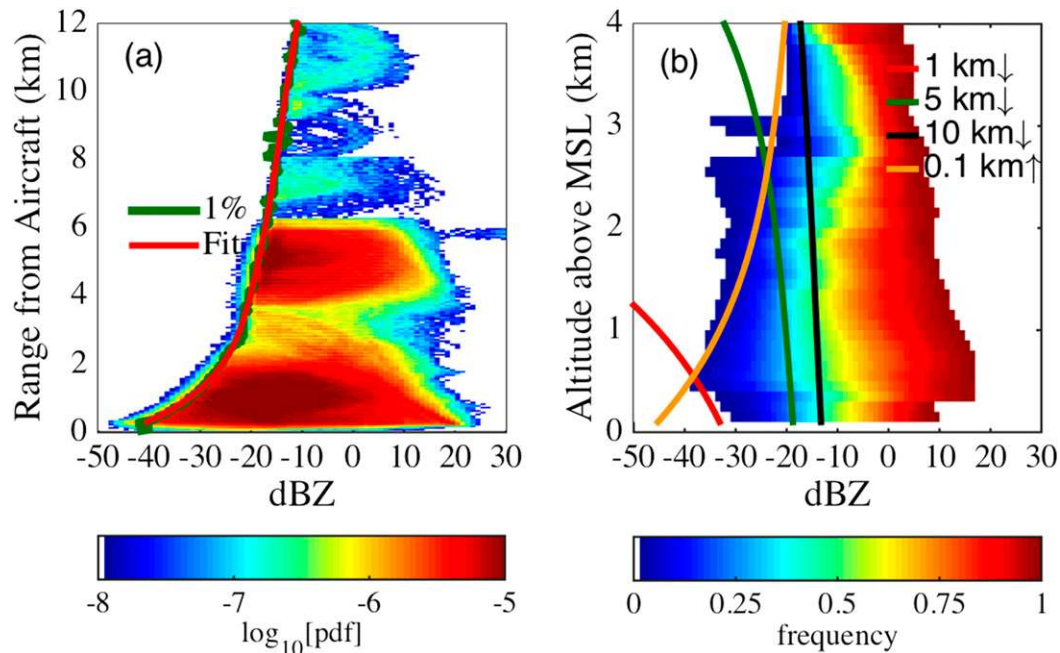
FIG. 3. (a) CFAD of reflectivity measured during level legs flown during CSET with respect to distance from the HCR. The 1st percentile of dBZ, conditional on distance, is shown by the green curve and the fit to it is shown in red. (b) Cumulative frequency of reflectivity measured between the sea surface and 4 km MSL, with the GV being no higher than 4 km MSL. The minimum detectable signal of the HCR at various GV altitudes and different pointing angles are shown. Upward arrow corresponds to zenith-pointing mode, and the downward arrow corresponds to nadir-pointing mode.

and 6 km reflect the CSET sampling strategy, with low-level sampling sequences conducted below 3 km and the ferry legs conducted at ~6 km. Several instances with reflectivity values greater than 0 and 10 dBZ, thresholds conventionally applied to identify periods of heavy drizzle (Comstock et al. 2007; Wood 2012), were recorded. The 1st percentile of the samples at each range gate and their best fit as a function of range are computed to describe the minimum detectable signal of the HCR at each range gate. After accounting for the attenuation expected as a square of the range, the measured reflectivity matches very well with HCR's theoretically calculated sensitivity of −39.6 dBZ at 1 km.

The cumulative distribution function of the HCR reflectivity observed below 4 km is shown in Fig. 3b, together with the profiles of HCR's minimum detectable signal at various GV altitudes and pointing angles. The nominal cloud-top heights of MBL clouds observed during CSET were between 1 and 2 km MSL. Based on data collected at ARM sites, warm boundary layer clouds can have reflectivity as low as −45 dBZ (Ghate et al. 2010, 2011, etc.). Figure 3b shows that during surface legs flown at 100–140 m MSL, the HCR was able to capture all the clouds below an altitude of 1 km while missing some nonprecipitating clouds at 2 km that did

not exceed the minimum detectable signal of −30 dBZ. At an altitude of 5 km or above, the HCR can only observe returns greater than −20 dBZ corresponding to drizzle. These results suggest that the HCR detects both nonprecipitating and precipitating boundary layer clouds when the GV is flying below 1 km but only precipitating boundary layer clouds when the GV is flying above 2 km.

During level legs, the GV makes small altitude adjustments to counter vertical air motions due to atmospheric turbulence. The reflector adaptively corrects for the changes in the platform motion at a 20-Hz resolution, referred to as the real-time pointing angle correction (Vivekanandan et al. 2015). In addition to the real-time pointing angle corrections, two further corrections are performed on the measured mean Doppler velocity: 1) the platform motion is corrected by subtracting the platform vertical air motion reported by the internal navigation system (INS) from the mean Doppler velocity at a 100-Hz resolution, and 2) the mean Doppler velocity of the surface echo is subtracted from the mean Doppler velocity. The mean Doppler velocity of the ground echo should be zero after making the first correction; however, it was nonzero representing the errors because of pointing angle offsets combined with errors

in vertical motion of the platform measured by the INS and the measurement variance of mean Doppler velocity. Hence, the second correction is made. Vivekanandan et al. (2015) provide a detailed description of the corrections.

The PDF of the mean Doppler velocities from the pulse-pair technique for cloud and precipitation echoes observed during the surface legs and above-cloud legs is shown in Fig. 4. Also shown is the INS-reported vertical motion of the HCR and the surface echo. A threshold of $-20\,\text{dB}Z$ is applied to distinguish between cloud and precipitation echoes. The mode of the vertical motion from cloudy samples ($\text{dB}Z < -20$) from both the upward- and downward-looking samples is less than zero ($-0.2\,\text{m s}^{-1}$), signifying downward motion, with the distribution being negatively skewed. This suggests some precipitation drops are still present in the samples even at the threshold of $-20\,\text{dB}Z$, similar to that reported by Luke and Kollias (2013). The mode and skewness of the distribution of mean Doppler velocity of precipitation drops are lower (more negative) than that of the cloud drops, suggesting it is the fall velocity of the precipitation-sized drops that dominate the mean Doppler velocity rather than the turbulence. In addition, several instances of positive mean Doppler velocities also occur, denoting updrafts in both cloud and precipitation samples.

The mean and the mode of the INS-reported vertical motion of the HCR was zero during both the upward- and downward-pointing modes, with the standard deviation of the distribution tending to be higher during the upward-pointing surface legs than during above downward-pointing cloud legs. This indicates that the atmosphere is less turbulent above the subcloud boundary layer, thereby requiring fewer altitude adjustments by the GV. The surface correction can only be made during the above-cloud (downward pointing) mode and is lower than the INS correction during that leg. Collectively these results show that the two corrections applied to the mean Doppler velocity could be at times comparable to the measurement itself, especially at the velocities weaker than $0.5\,\text{m s}^{-1}$ that are characteristic of the cloud droplets observed during surface legs.

The measured width of the Doppler spectrum during nadir- or zenith-pointing modes includes contributions from the hydrometeor drop size distribution σ_{dsd}, wind shear σ_s, turbulence σ_t, and beam-broadening σ_b. Chu (2002) and Chen and Chu (2011) derived the theoretical contribution to the beam broadening as a function of the wind speed for ground-based radars using the original formulation by Sloss and Atlas (1968). Here, we use their following formulation during zenith- and nadir-pointing modes:
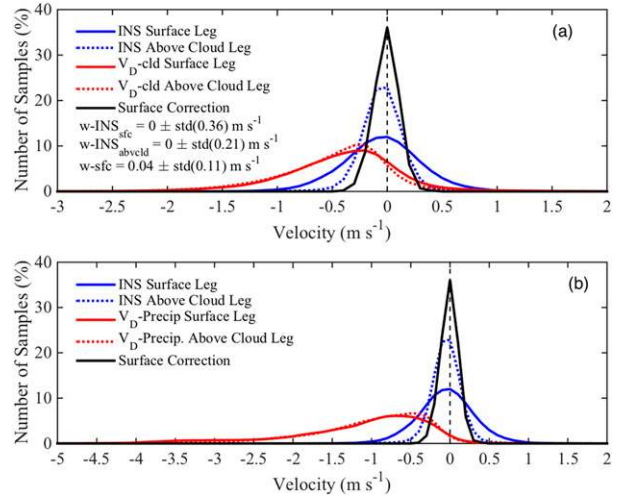

FIG. 4. (a) Histogram of INS-reported HCR vertical velocity (blue) and mean Doppler velocity of cloudy samples (red) from all of the surface legs (solid) and above-cloud legs (dashed) during CSET. (b) As in (a), but for precipitation samples. The surface correction (black) is shown in both panels. The mean and standard deviation of INS-reported platform vertical motion and surface correction are also reported. This figure was made using v_D calculated using the pulse-pair technique. Estimates of v_D calculated using the spectral technique showed similar values.

$$\sigma_b = \frac{U\theta}{2\sqrt{\log 2}}, \qquad (1)$$

where U (m s^{-1}) is the aircraft speed and θ (rad) is the half beamwidth of the radar ($0.34°$ for the HCR). After correcting for the broadening due to platform motion, the Doppler spectrum width can in theory be used to retrieve turbulence dissipation rates (Fang et al. 2014; Albrecht et al. 2016; Borque et al. 2016) and, as reported here, the drizzle drop size distribution when combined with the HSRL data (O'Connor et al. 2005). The GV speed of $\sim\!130\,\text{m s}^{-1}$ during low-level sampling legs and $\sim\!220\,\text{m s}^{-1}$ during ferry legs correspond to width corrections of 0.46 and $0.79\,\text{m s}^{-1}$, respectively.

Before performing echo classification and microphysical retrievals from the moments of Doppler spectra, it was essential to determine whether to use estimates calculated from the pulse-pair or the spectral technique. Histograms of Doppler spectrum width calculated using the pulse-pair technique and the spectral technique for both cloudy and precipitation samples are shown in Fig. 5. The distribution of the contribution from aircraft motion to the spectrum width is also shown. This is subtracted from the calculated spectrum width to produce estimates that are used to retrieve microphysical properties (section 4). Unlike the mean Doppler velocity, the spectrum width estimates from the pulse-pair and spectral technique do not agree with each other,
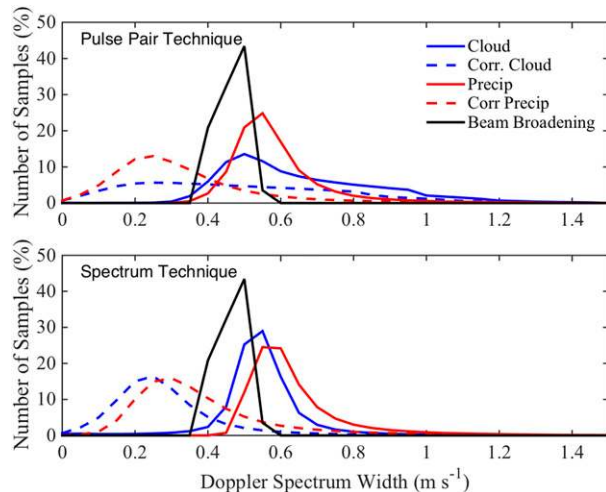
FIG. 5. Histogram of the width of the Doppler spectrum calculated using (top) the pulse-pair technique and (bottom) the spectrum technique. Shown are the histograms of raw (solid) and corrected (dashed) spectrum width for cloud samples (blue) and precipitation samples (red) during all of the CSET surface and above-cloud legs. Shown in both panels is the histogram of broadening due to aircraft motion (black).

with the estimates from pulse-pair technique exhibiting greater range and spatial variability than those from the spectral technique, particularly true for clouds. The observed widths are always greater than the theoretically estimated broadening due to aircraft motion. After correcting for the broadening due to aircraft motion, the mean spectral width of cloud and precipitating samples from the spectral technique is 0.36 and 0.48 m s^{-1}, respectively, while these values derived from the pulse-pair technique are 0.57 and 0.44 m s^{-1}, respectively. It is beyond the scope of this article to investigate the causes of these differences. After correcting for beam broadening, the spectrum width has contributions from wind shear, turbulence, and drop size distribution. On average, we anticipate the wind shear and turbulence to be similar within cloudy and precipitation samples yielding higher values of spectrum width for precipitation samples than the cloudy samples. However, the mean spectrum width, calculated from pulse-pair technique, of cloudy samples is greater than that of precipitation samples. Thus, for the retrievals in this study, we use the estimates of spectrum width calculated from the spectral technique.

3. Hydrometeor mask and classification

An example of data collected by the HCR and HSRL during the last low-level sampling legs and the ferry leg back to Sacramento on RF11 (29 July 2015) is shown in Fig. 6. The HCR and the HSRL beams pointed upward during the surface legs and pointed downward during the above-cloud, in-cloud, and porpoise legs. During the surface legs (flown at ~100 m), similar to ground-based radars and lidars, the HCR can observe the full vertical structure of the cloud and precipitation layers, and the HSRL observes the precipitation below cloud base and the cloud-base height. The peak in the HSRL backscatter (orange colors) during the surface leg when the HSRL was pointing upward refer to the cloud-base height. During the in-cloud legs, the HSRL attenuates completely within the first few range gates except during optically thin veil clouds described in Wood et al. (2018), and the HCR observes the precipitation below the cloud base. As the dead zone of the HCR is 203 m, the HCR does not record any returns when the hydrometeor base is less than 203 m away from the GV. During the above-cloud legs, typically flown within 1 km of the cloud top, the HSRL records the cloud-top height, and the HCR observes the cloud and the precipitation structure. Because of reduction in the minimum detectable signal with range, the HCR is only sensitive to drizzle echoes during the 6-km-altitude ferry flights (see also Fig. 3), while the HSRL becomes fully attenuated at the top of boundary layer clouds.

a. Hydrometeor mask

To accurately estimate the hydrometeor mask, it is essential to merge the data from the HCR and the HSRL. By using the INS-reported GV altitude, and the elevation angle of the HCR, the HCR moments are converted to a time–height grid beginning at the mean sea level and at 2-Hz temporal and 20-m range resolutions. A similar procedure is applied to the HSRL data, to generate a merged dataset extending from the surface to 14 km at 2-Hz temporal and 20-m height resolutions for all of the CSET research flights. Calibration of the HCR and HSRL is mostly performed during the ferry flights, and data from these periods are manually identified and not included in the merged dataset. Also, at times, the INS suffered from technical issues and needed to be restarted, yielding gaps in the HCR and INS data lasting a few minutes during some flights. Data collected during these periods are also not included in the merged dataset.

The HSRL is sensitive to both aerosol and hydrometeors, so it is essential to identify the HSRL returns that correspond to hydrometeors only before merging the HSRL data with that from the HCR. The procedure described by Kotthaus et al. (2016) is largely followed to distinguish between aerosol and hydrometeor returns. Segments of cloud-free areas, typically above the boundary layer in the areas where low-level sampling is
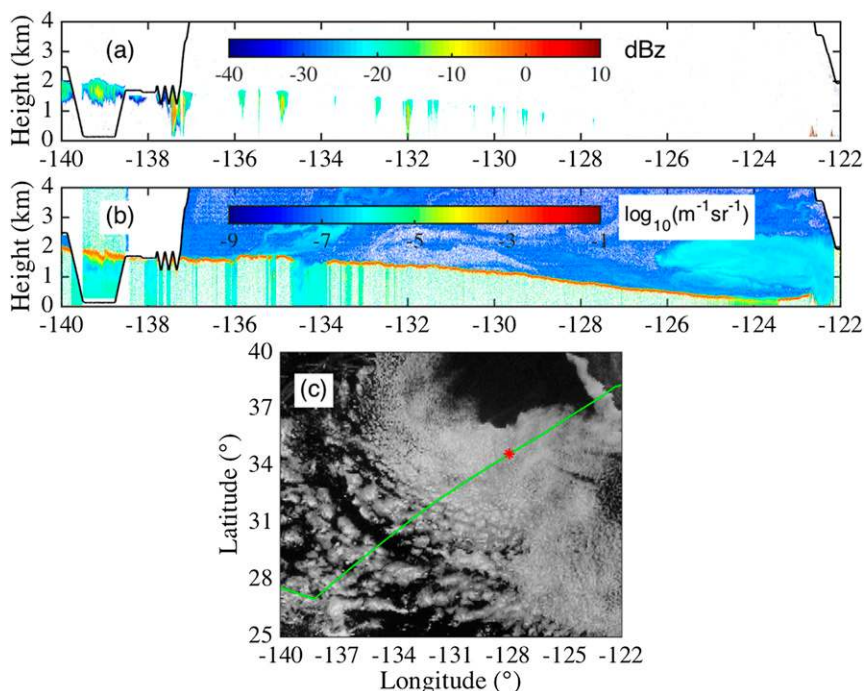
FIG. 6. Example of data collected between 2049 and 2354 UTC 29 Jul 2015 (RF11). Shown are (a) the longitude–height plot of HCR reflectivity, (b) the longitude–height plot of HSRL-reported backscatter, and (c) the GOES visible imagery during the period. The GV altitude is shown in black in (a) and (b). The GV track is shown in green in (c), with the red asterisk indicating GV location when the GOES image was captured. The GV altitude during the ferry flight, not visible in (a) and (b), was around 6.7 km. Similar plots for the entire flight duration for all of the research flights made during CSET are included in the online supplemental material.

conducted, are manually identified for each flight, and the average is calculated of the lowest 1% of HSRL-reported aerosol backscatter cross section. This value is deemed as the background aerosol backscatter for that flight. The background aerosol backscatter values calculated by averaging the lowest 2% or 5% of the samples do not substantially affect the identification of the hydrometeors returns much. The HSRL-reported particulate backscatter for the entire flight is then divided by the background aerosol backscatter and converted to decibels (dB). The aerosol returns are then distinguished from those from hydrometeors using a threshold dB value for each flight. The mean of the threshold used for distinguishing aerosol returns from hydrometeor returns is 25 dB. For some of the flights (e.g., RF02), a higher threshold was warranted because of the presence of aerosol plumes resulting from forest fires (Albrecht et al. 2019). The thresholds used for distinguishing aerosol and hydrometeor returns from the HSRL data for each flight are reported in the supplemental material. A more comprehensive technique that uses HSRL-reported linear depolarization ratio (LDR) and extinction coefficient will be needed for distinguishing aerosol

and hydrometeor returns during cirrus and mixed-phase cloud conditions.

After identifying significant returns from the HSRL and HCR to generate the hydrometeor mask for each flight, the speckled noise is removed using a spatiotemporal filter (Clothiaux et al. 2000). If fewer than four of the surrounding eight pixels of a chosen pixel have significant returns, then the chosen pixel was determined to be clear. As a result, cloud elements shorter than 1.5 s wide (~300 m long) and 60 m tall are discarded. Given the fast-moving platform, and sensitivity of the HCR, we believe this to be the optimal filter size. The HCR and HSRL hydrometeor masks are then merged by finding their union, yielding boundaries of hydrometeor layers. As the HSRL was pointing 4° off of the fuselage toward the left wing when pointing downward, and the HCR was pointing directly downward from the right wing, they might not have been observing the same cloud elements during above-cloud and ferry legs. The HSRL beam was 69.93 m away from the HCR beam for a target 1 km below GV (above-cloud legs) and 419.56 m away from the HCR beam for a target 6 km below the GV (ferry legs). As marine stratocumulus clouds have cell
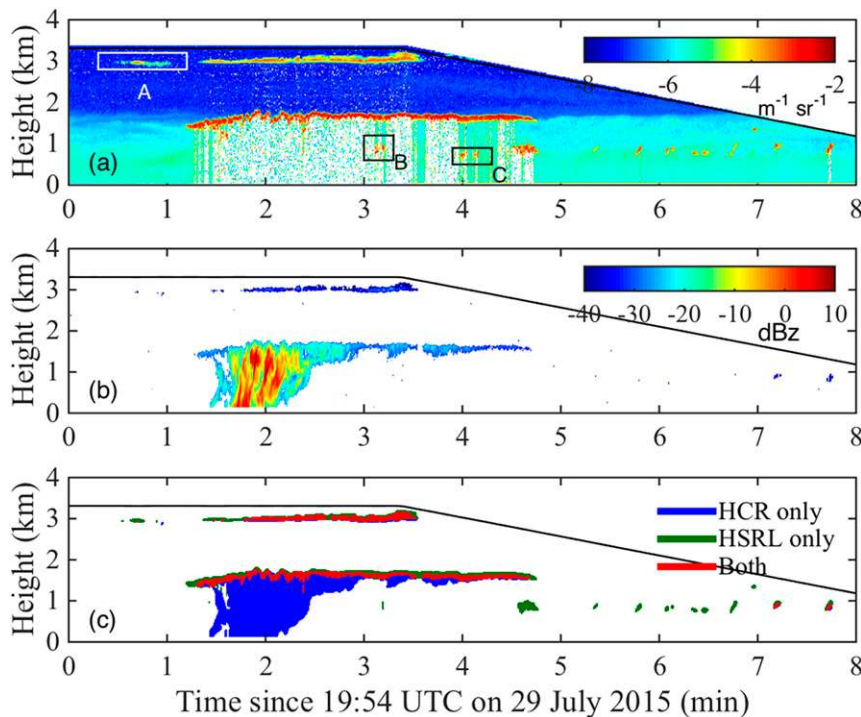
FIG. 7. Time–altitude plot of (a) HSRL-reported backscatter, (b) HCR-reported reflectivity, and (c) the combined hydrometeor mask for an 8-min period during RF11. The HIAPER altitude is shown as a black line in all panels. The features labeled A, B, and C, discussed in the text, are shown in (a).

size of 30–40 km (e.g., Wood and Hartmann 2006), we anticipate the HSRL and HCR to be observing the same cloud element in the stratocumulus region. However, as shallow cumulus clouds often have diameters of ~500 m (e.g., Lareau et al. 2018), it is possible for the HCR and the HSRL to be observing a different cloud element, especially during ferry legs flown at ~6 km.

For below-cloud flights, the lowest cloud layer's base is determined by finding the maximum gradient in the HSRL backscatter (Kovalev and Eichinger 2004). A hydrometeor mask data product (Ghate et al. 2016) is produced that includes the merged masks, derived cloud-base height from the gradient method, echo boundaries, first three moments of the Doppler spectra, and the HSRL backscatter on a uniform georeferenced time–height grid. The noise-filtered values of radar reflectivity, HSRL backscatter, and visible satellite imagery within 2° of the GV are produced for the entire duration of each flight (similar to Fig. 6), and those images are included in the supplemental material.

An example of the merged hydrometeor mask is shown in Fig. 7 for a time period that includes both thin veil clouds (top at ~3 km), precipitating stratocumulus clouds (top at ~1.8 km), and shallow cumulus clouds (top at ~1 km). The HSRL beam is able to penetrate

through the optically thin veil clouds and also observe the thin shallow cumulus clouds. The thin veil clouds are only occasionally thick enough to be observed by the HCR. Cloud feature A corresponds to a thin veil cloud that the HSRL beam can penetrate. However, the feature is less than 60 m thick at times, particularly toward the horizontal edges and hence is not fully captured by the hydrometeor mask (Fig. 7c). Features B and C correspond to shallow cumulus clouds beneath a precipitating stratocumulus cloud deck. These clouds are observed by the HSRL as the stratocumulus cloud above is thin, but they are missed by the HCR because of low sensitivity. The clouds in B and C are thicker than 60 m; however, they are intermittent, with sampling gaps that are less than 1.5 s in width. Hence, they are removed by the spatial–temporal filter and are not captured by the hydrometeor mask. Despite these shortcomings, the merged hydrometeor mask captures the cloud and precipitation structure better than either instrument alone.

b. Hydrometeor classification

An essential step for determining the cloud fraction and cloud boundaries and for retrieving microphysical properties is to first classify the echoes as cloud (with or without precipitation) or precipitation only. This is
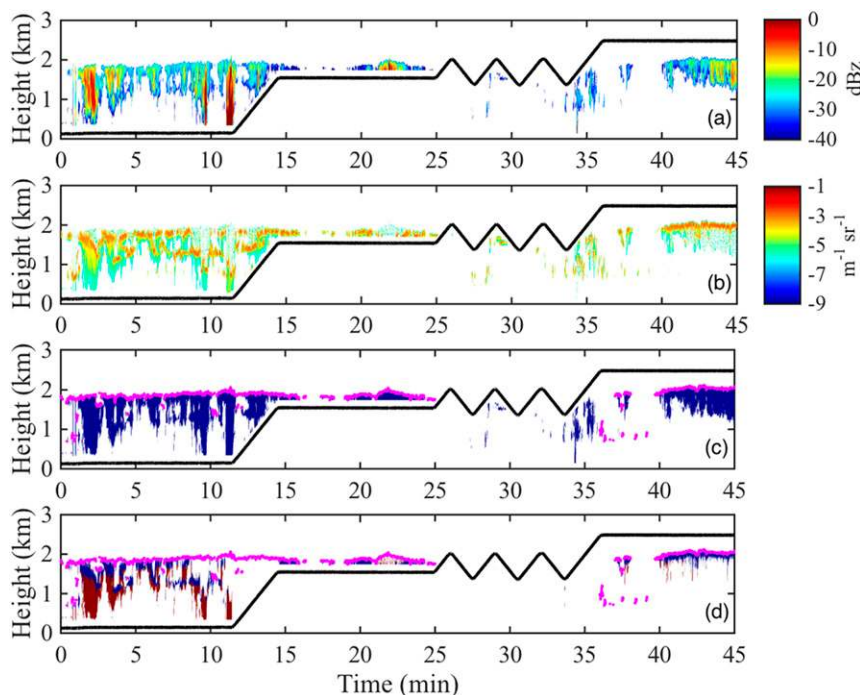
FIG. 8. Time–height profiles of (a) HCR reflectivity, (b) HSRL backscatter, (c) HCR–HSRL-merged hydrometeor mask, and (d) hydrometeor class with cloud samples shown in blue and precipitation samples shown in red. The GV altitude (km MSL) is shown in all panels (black line). The cloud-top height of the highest cloud layer in the boundary layer is shown in (c) and (d) (magenta). For clarity, samples classified as "mixed" are not shown in (d). The example is from RF11 that was made on 29 Jul 2015, and the start time (time 0) corresponds to 2005:00 UTC. The HCR and HSRL were pointing upward during surface and in-cloud legs and downward during the porpoise and above-cloud legs.

achieved using a fuzzy logic method (Vivekanandan et al. 1999). Fuzzy logic allows for the weighing of the possibilities of multiple classifications (Mendel 2001) based on noisy remote sensing measurements that depend neither linearly nor uniquely on the scene being observed (Liu and Chandrasekar 2000). There are several fuzzy logic methods of varying complexities used in the literature. Here, a simple rule-based fuzzy logic inference method based on Mendel (2001) is adopted (details in the appendix). The HCR-reported mean Doppler velocity, HSRL-reported calibrated backscatter, and the ratio of the HCR reflectivity to HSRL backscatter provide the inputs to the fuzzy logic technique. In our definition, the "cloud" category can contain precipitation; however, the "precipitation" category does not contain any cloud drops. Data collected below and above the cloud base during single-layered stratocumulus cloud conditions from RF07 are used to determine the membership functions, and the cloud and precipitation classes strictly refer to hydrometeors above and below cloud base, respectively. Samples that cannot be classified as cloud or precipitation are labeled as "mixed."

An example of the fuzzy logic output is shown in Fig. 8 for a low-level sequence made during RF11 on 29 July 2015. Shallow cumulus clouds below precipitating stratocumulus are observed during the surface leg, and single-layered precipitating stratocumulus clouds are observed during the above-cloud leg. The GV vertical air motion is substantial during the porpoise legs, overwhelming the HCR-reported mean Doppler velocity. This disqualifies data collected during porpoise legs from the fuzzy logic hydrometeor classification technique. When the HSRL and the HCR data are simultaneously available, the technique identifies multiple cloud layers and discriminates between the cloud and precipitation volumes. A simple threshold on HCR reflectivity does not capture the true structure of the scene, and a simple threshold on either HSRL backscatter or its gradient generates a noisier cloud base and hydrometeor classification.

As seen in Fig. 8 (during minutes 9–11), a fuzzy logic system that makes use of both the HCR and the HSRL measurements fails when the HSRL signal attenuates in optically thick cloud. When the GV is flying above cloud and viewing in the nadir direction, fuzzy logic also fails

in identifying the cloud base except when the cloud is optically thin. For this reason, it is desirable to have a fuzzy logic system that can discriminate between cloud and precipitation using only the HCR data. Initial attempts at using only the HCR datasets produce classifications that appear to be converging on the correct solution, but these retrievals are still insufficient. Our analysis does reveal, however, that the width and skewness of the Doppler spectra that are deconvolved to remove broadening due to aircraft motion will significantly improve the classification based on HCR data only. This effort is ongoing and is discussed in the summary section.

The hydrometeor mask (cloud top and base for multiple clouds within the vertical column) and the hydrometeor class (cloud, precipitation, or mixed) are reported in the same data product that reports the HCR moments and the HSRL backscatter on a georeferenced uniform 2-Hz temporal and 20-m vertical resolutions. One file is produced for each flight. An instrument flag variable is included in the file that informs the user if the particular grid cell was observed by neither the HCR or HSRL (values set to zero), HCR only (value set to 1), HSRL only (value set to 2), or both the HCR and HSRL (value set to 3). The hydrometeor class variable also has dimension similar to the hydrometeor mask (and the radar moments) with the value set to 0 for clear air, 1 for cloud, 2 for precipitation, and 3 for mixed.

4. Microphysical retrievals

One of the primary objectives of CSET is to understand the role of precipitation in causing the transition from a stratocumulus to cumulus cloud regime. Several techniques have been proposed to retrieve the cloud and drizzle microphysical properties at various temporal and range resolutions. Some of the retrieval techniques use moments of Doppler spectra from a cloud radar and LWP (e.g., Frisch et al. 1995; Frisch et al. 2002), or the Doppler spectra and the LWP (e.g., Luke and Kollias 2013), or use moments of Doppler spectra, LWP, and irradiances in the shortwave spectrum (e.g., Fielding et al. 2015; Dong and Mace 2003). In this study, the drizzle microphysical properties are retrieved by combining the data from the HSRL and HCR similar to that done by O'Connor et al. (2005), highlighting the information content of the two remote sensors onboard the GV. Thin veil clouds associated with ultraclean layers are routinely observed during CSET (Wood et al. 2018). Therefore, an algorithm to retrieve their microphysical properties is also developed. Below are the details of both techniques along with some examples of their application.

a. Drizzle retrievals

The HSRL backscatter β and the radar reflectivity Z is proportional to the second and sixth moment of the drop size distribution, respectively. Hence, the ratio of the two Z/β is proportional to the fourth power of the hydrometeor diameter. This is largely the basis of the O'Connor et al. (2005) technique that retrieves parameters of the drizzle drop size distribution based on calibrated values of ceilometer backscatter and radar reflectivity. Similar to Testud et al. (2001) and Smith (1982), we assume drizzle can be represented with a normalized gamma-shaped drop size distribution with three parameters (N_w, μ, and D_0):

$$n(d) = N_w f(\mu)\left(\frac{d}{D_0}\right)^{\mu}\exp\left[\frac{-(3.67+\mu)d}{D_0}\right],$$

$$f(\mu) = \frac{6}{3.67^4}\frac{(3.67+\mu)^{4+\mu}}{\Gamma(\mu+4)}. \tag{2}$$

The parameters of the gamma distribution are reflected within the reflectivity to the backscatter ratio and the width of the Doppler spectrum:

$$\frac{Z}{\beta} = \frac{2}{\pi}\frac{\Gamma(7+\mu)}{\Gamma(3+\mu)}\frac{S(D_0,\mu)\gamma'(D_0,\mu)}{(3.67+\mu)^4}D_0^4, \tag{3}$$

$$\sigma_D^2 = \frac{a^2D_0^2(\mu+8)(\mu+7) - a^2D_0^2(\mu+7)^2}{(3.67+\mu)^2}. \tag{4}$$

Equations (3) and (4) are solved iteratively to retrieve D_0, which then is used within Eq. (5) to retrieve the normalized number concentration N_w:

$$Z = N_w f(\sigma D)D_0^6\sigma De^{18\sigma D^2}. \tag{5}$$

The lidar ratio S and Mie-to-Rayleigh backscatter ratio γ' are calculated using forward-modeled extinction and backscatter efficiencies at 532- and 3.2-mm wavelengths (Wiscombe 1980). The constants a and b in Eq. (4) correspond to the diameter to fall-velocity relationship proposed by Gossard et al. (1990) with $a = 1.2 \times 10^{-4}$ s and $b = 1 \times 10^{-5}$ s. The width of the Doppler spectrum is corrected for the broadening due to aircraft motion before being applied within Eq. (4). Propagating the uncertainty of 1.5 dB (40%) for the reflectivity and 10% for the HSRL backscatter, we estimate the uncertainty in the retrieved drizzle liquid water content (LWC) to be 14% and in the modal diameter to be 9%.

An example of the retrieved drizzle LWC and effective diameter D_{eff} is shown in Fig. 9. The aircraft was flying below a drizzle shaft during this period. The LWC decreased from the cloud base to the surface, while the
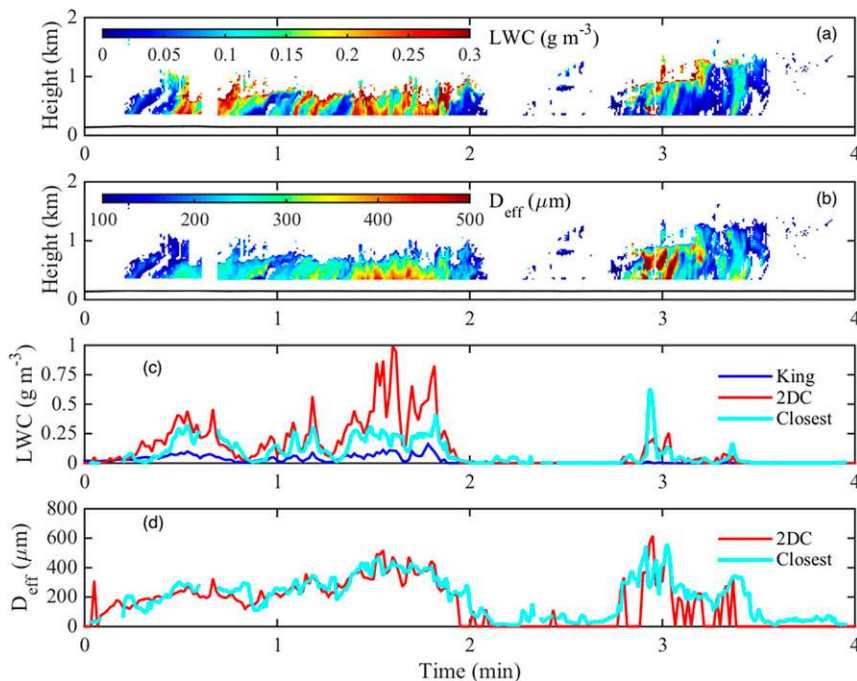
FIG. 9. Time–height profiles of (a) drizzle liquid water content and (b) effective diameter. Comparison of the (c) retrieved liquid water content and (d) effective diameter closest to the aircraft to that reported by situ instruments. The GV altitude is shown in (a) and (b). This example is from RF07 made on 19 Jul 2015, with a start time (time 0) of 1933 UTC. The average aircraft speed and altitude during this period was 127.03 m s^{-1} and 145.47 m, respectively.

effective diameter increased from the cloud base to the surface, consistent with the evaporation of smaller drizzle drops in a subsaturated environment. The retrieved LWC closest to the aircraft (at 203 m) is similar to that measured by the two-dimensional cloud (2DC) probe, except for directly underneath the drizzle shaft, and is higher than that measured by the King probe that is known to underestimate contribution of large drops to LWC (Biter et al. 1987). The differences between the 2DC reported and the retrieved LWC between 1 and 2 min could be simply due to drizzle evaporation within the lowest 203 m or the differences in the sampling volume of the two instruments. The effective diameter retrieved closest to the aircraft is very similar to that measured by the in situ 2DC probe, which is capable of resolving the sizes of drops between 62.5 and 3187.5 μm.

The scatterplots between closest retrieved drizzle LWC and drizzle D_{eff} with that measured by the 2DC probe during all of the surface legs at 1-s resolution (blue dots) and averaged over the entire leg (red square) are shown in Fig. 10. A total of 61 surface legs were flown during CSET, and of these, 32 exhibited drizzling cloud conditions. Only periods when the retrievals were available and the 2DC also detected drizzle were included in this analysis. Generally, there is a good

agreement with the 2DC-reported and the closest retrieved values with higher scatter for 1-s data than the leg-averaged data. These differences could be due to differences in sampling volume and drizzle evaporation. In addition, the GV travels at ~125 m s^{-1} during surface legs, which, coupled with shear in horizontal winds, could lead to sampling of the hydrometeors from different clouds by the 2DC and the remote sensing instruments. The root-mean-square difference calculated from the leg-averaged values between the closest retrieved LWC and that measured by 2DC was 0.08 g m^{-3}, and the same for D_{eff} was 37.94 μm. The average in situ and closest retrieved LWC between the ranges of 0.01 and 0.1 g m^{-3} were both 0.5 g m^{-3}. The root-mean-square difference between the two measurements within this range was 0.03 g m^{-3}, 6% of the in situ–reported value.

b. Cloud retrievals

Optically thin veil clouds were routinely observed during CSET (Wood et al. 2018). The HSRL beam can penetrate the thin clouds; however, because of low droplet concentrations, they have very low reflectivity that was often below the sensitivity of the HCR. These thin clouds are identified using the merged hydrometeor mask data (section 3) by identifying cloudy range gates
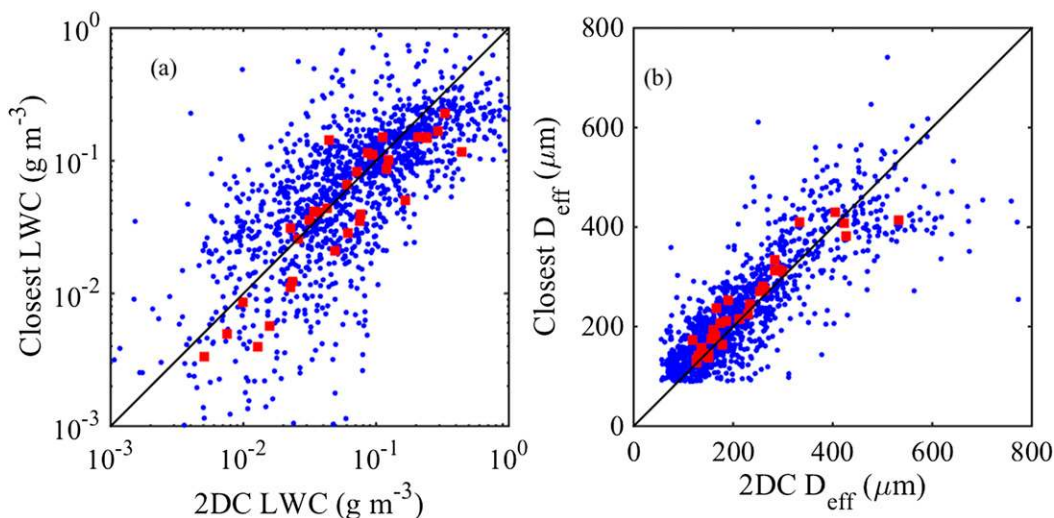
FIG. 10. Scatterplot between (a) the closest retrieved LWC and that measured by 2DC and (b) the closest retrieved effective diameter and that measured by the 2DC. The 1-s data are shown as blue dots, and the leg-averaged data are shown as red squares.

that did not completely attenuate the HSRL beam. The parameters of the cloud drop size distribution cannot be retrieved using the HSRL data alone. Hence, during periods when the thin clouds are observed by both the HCR and the HSRL, we assume the clouds to follow a lognormal drop size distribution normalized for liquid water content (Testud et al. 2001), with modal diameter D_m, total droplet concentration N_w, and width σ. The width of the distribution is assumed to be 0.38 (Frisch et al. 1995; Miles et al. 2000):

$$n(D) = \frac{N_w f(\sigma)}{D\sqrt{2\pi}} \exp\left\{ \frac{-[\ln(D/D_m)]^2}{2\sigma^2} \right\},$$
$$f(\sigma) = \frac{e^{-(9/2)\sigma^2}}{\sigma}. \tag{6}$$

The ratio of the radar reflectivity to lidar backscatter [Eq. (7)] then yields the modal diameter, similar as is done for drizzle. The modal diameter is then used to calculate the number of cloud drops from the reflectivity:

$$\frac{Z}{\beta} = S\gamma'\frac{2}{\pi}D_m^4 e^{16\sigma^2}. \tag{7}$$

In Eq. (7), the lidar ratio S is typically 18.63 sr. Because of the small drop diameter, the Mie-to-Rayleigh backscatter ratio γ' was always unity. An example of the retrieved microphysical properties and their comparisons with those measured by in situ sensors are shown in Fig. 8 of Wood et al. (2018). As the veil clouds were often not thicker than 203 m, there were only three

instances when the retrievals were made and the Cloud Droplet Probe (CDP) also detected the clouds. In addition, the veil cloud was only observed for a few minutes during porpoise legs while going in and out of the boundary layer. Hence, it was not possible to perform statistical comparison between CDP measured and closest retrieved cloud microphysical properties.

5. Summary, potential applications, and future work

To gain insights into key processes affecting the transition from stratocumulus to cumulus cloud regime, the Cloud System Evolution in the Trades (CSET) campaign was conducted in the summer of 2015. Fourteen transects were made between Sacramento, California, and Kona, Hawaii, collectively sampling the quasi-Lagrangian evolution of 18 air masses with a 2-day lag. CSET was the first full deployment of both the HCR and the HSRL together to observe marine boundary layer clouds. The raw in-phase (I) and quadrature (Q) components of the received digitized signal were recorded for the entire campaign, making it possible to calculate the Doppler spectra and its moments at any desired temporal resolution. Our analysis reveals 0.5 s is the optimal temporal resolution for calculating the Doppler spectra and its moments and that these are suitable for retrieving cloud and precipitation macro- and microphysical properties. Because of the HCR's sensitivity of -39 dBZ at 1 km, the HCR is mostly able to observe drizzle shafts, except during the surface legs made at 100–140 m above sea level. The broadening of
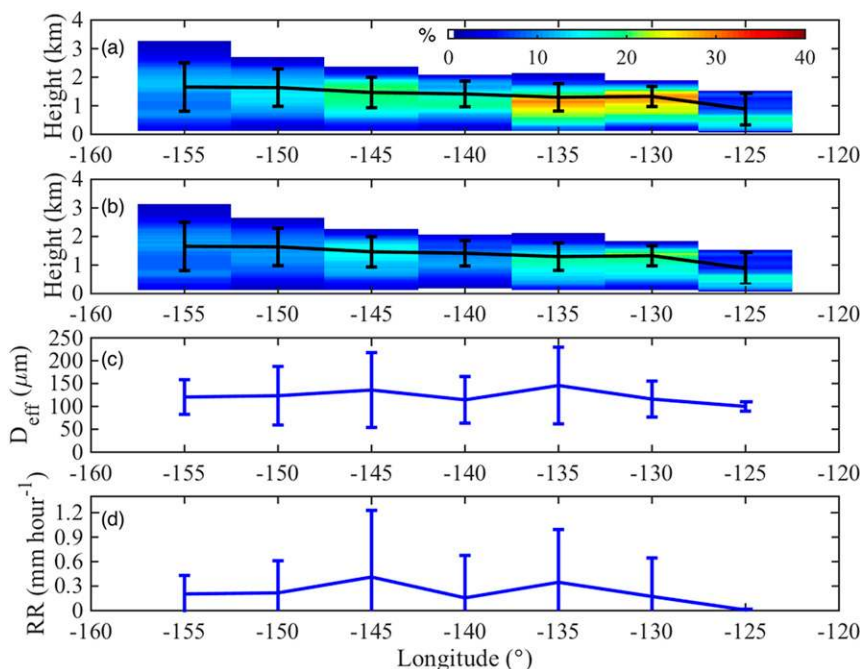
FIG. 11. (a) Average hydrometeor fraction binned by longitude (colors) and the average boundary layer cloud-top height (black line) as observed during the entire CSET campaign. (b) Average rain fraction binned by longitude (colors) and the average boundary layer cloud-top height (black line) as observed during the entire CSET campaign. (c) Drizzle effective diameter D_{eff} at the cloud base retrieved during the surface legs binned by longitude. (d) Rain rate at the cloud base retrieved during the surface legs binned by longitude. The vertical bars in all panels denote one standard deviation from the mean. The color scale for (a) and (b) is shown in (a).

the Doppler spectrum width is ~0.46 m s^{-1} during low-level sampling legs because of the GV speed of ~130 m s^{-1}. This invalidates proposed techniques for retrieving turbulence profiles and entrainment rates in nonprecipitating stratocumulus clouds, based on the spectrum width and the mean Doppler velocity (Fang et al. 2014; Albrecht et al. 2016), because ground-based observations have revealed the spectrum width in nonprecipitating stratocumulus clouds to be ~0.5 m s^{-1}. Because of the uncertainty in the HCR-reported mean Doppler velocity and the significant contribution of the aircraft motion to the spectrum width, we anticipate the retrievals of turbulence and entrainment rates can only be made for CSET after deconvolving the Doppler spectra to mitigate the aircraft motion.

The data from the HCR and the HSRL are combined for the purpose of detecting hydrometeor occurrences on a uniform georeference grid. After combining the data from the two instruments, the echoes are classified as cloud or precipitation using a fuzzy logic technique. This technique fails during instances when the HSRL beam is completely attenuated and is most successful during the low-level legs during when both the HCR and

HSRL were pointing upward. The skewness and kurtosis of the Doppler spectra can be used to detect the onset of precipitation (Kollias et al. 2011), although we suspect a fuzzy logic technique based on the moments calculated from Doppler spectra deconvolved for aircraft motion will be more successful in echo classification and microphysical retrievals. The detailed hydrometeor class and the microphysical retrievals available during low-level legs can be used in studies focused on boundary layer processes, while the hydrometeor mask available during the entire flights can be used for understanding large-scale changes in cloud and precipitation across the study region.

The detailed aerosol, cloud, and precipitation measurements made during CSET will yield new understanding of the cloud transitions in the North Pacific trades. Here, we provide two examples of ways in which the produced dataset can be used. Shown in Fig. 11 is the hydrometeor fraction, rain fraction, drizzle modal diameter at the cloud base, and rain rate at the cloud base binned by longitude calculated from observations made during the entire campaign at all vertical levels. For these calculations, the HCR returns greater than −20 dBZ
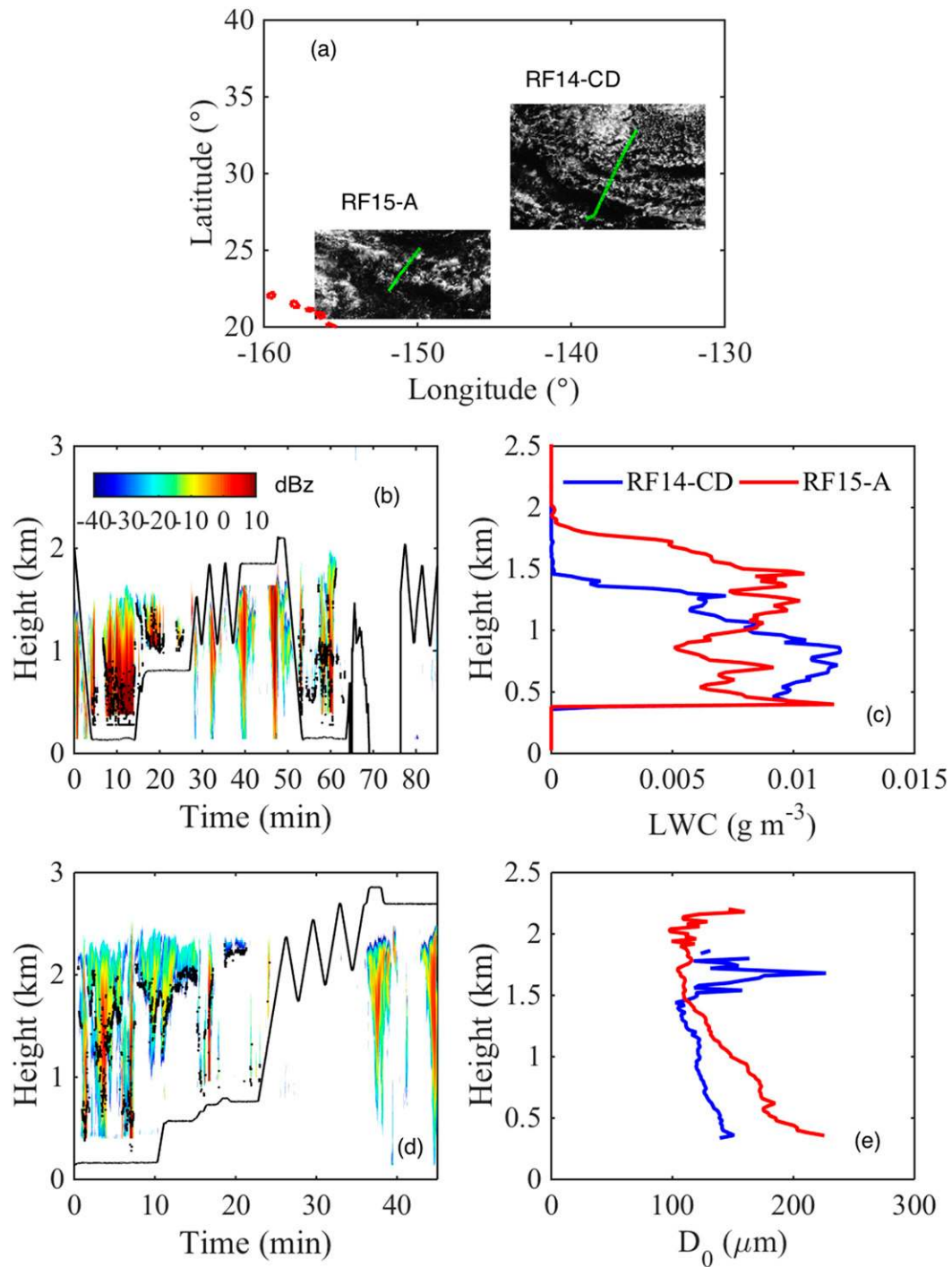
FIG. 12. (a) Visible satellite imagery during RF14-CD and RF15A. The GV track is shown in green. RF15A corresponds to the same advected mass sampled during RF14-CD. (b),(d) GV altitude (black line), HSRL-reported cloud-base height (black dots), and HCR-recorded radar reflectivity during RF14-CD and RF15-A, respectively. (c),(e) Average drizzle liquid water content and drizzle drop diameter observed during the surface legs of the two sampling sequences.

were used to calculate the rain fraction, rather than those satisfying the hydrometeor mask, to increase the available sample size. The boundary layer deepened from east to west with increase in the cloud-top heights and decrease in the cloud and rain fraction. The average drizzle effective diameter at the cloud base varied between 100 and 150 μm from east to west but exhibited considerable variability in each longitudinal bin, consistent with mesoscale variability of these clouds. The cloud-base rain rates were relatively low ($\sim$0.3 mm h^{-1}), consistent with the view of precipitation being ubiquitous in these cloud systems. The variability in aerosol, cloud, and precipitation properties from California to Hawaii as observed during CSET is explored further in Bretherton et al. (2019).

Because of the quasi-Lagrangian nature of the measurements made during CSET, the dataset could also be used to understand evolution of the cloud and precipitation structure over a 2-day period. Shown in Fig. 12 are observations made during two low-level sampling sequences on RF14 (C and D) and one low-level sampling sequence from RF15 (A) that correspond to the same air mass. Hence, the RF15-A observations report the natural evolution of the cloud and boundary layer structure from RF14-CD when forced with changes in external factors like increased SST and lower large-scale subsidence. Previous studies have focused upon aerosol source variability as the key driver of variability in the cloud radiative properties; however, recent studies have shown even light precipitation to be a key modulator of cloud radiative properties through aerosol scavenging (e.g., Wood et al. 2012). The accumulation mode aerosol concentration (0.1–1 μm) increased for this transition from $\sim$95 to $\sim$158 cm^{-3}, suggesting new aerosol sources, perhaps from surface fluxes.

The analysis presented here can eventually pave the way to retrieve drop sizes in thin clouds from satellite data by merging data from the Cloud Profiling Radar (CPR) and the Cloud–Aerosol Lidar with Orthogonal Polarization (CALIOP), satellite-based instruments that operate at frequencies similar to that of the HCR and HSRL, respectively. A further application of the HSRL dataset, which is otherwise not discussed here, is to characterize the radiative properties of the different aerosol species observed during CSET (Albrecht et al. 2019) through the lidar depolarization ratio, an application that benefits from the aerosol fields being less spatially variable than the cloud fields.
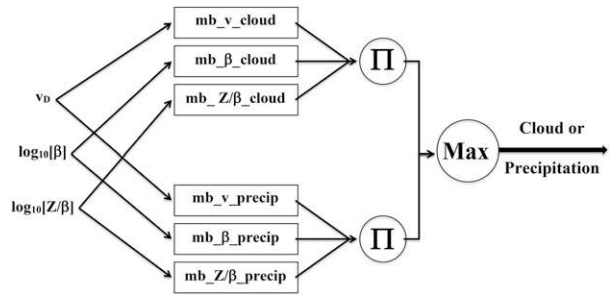
FIG. A1. Schematic diagram showing the method to determine cloud or precipitation samples using the observed mean Doppler velocity v_D, HSRL backscatter β, and the ratio of reflectivity to backscatter Z/β.

APPENDIX

Details of Fuzzy Logic Method

Generally, first in a fuzzy logic technique, "crisp" inputs (in this case, remote sensing observations) are first "fuzzified" to account for their uncertainty. Then a set of rules are applied to the fuzzified inputs in order to determine the values of their memberships within each of a group of fuzzy output sets. And finally, defuzzification is performed to produces a crisp output—a decision as to which fuzzy output set the crisp inputs belong—based upon the determined memberships (Mendel 2001).

The fuzzy logic method implemented here (illustrated in Fig. A1) follows that of Liu and Chandrasekar (2000). Remote sensing observations are taken as inputs and operated on with a "fuzzy singleton" (Mendel 2001), passing perfunctorily through fuzzification as hard values with no treatment of their uncertainty. Then each rule is used to infer the membership of each remote sensing measurement in either a "cloud" fuzzy set or a "precipitation" fuzzy set. For instance, the rule pair for mean Doppler velocity v_D from the HCR is as follows:

TABLE A1. Parameters used in the fuzzy logic classification system and the membership functions.

Measurement	Units	Parametric form	Cloud	Precipitation
v_D	m s^{-1}	beta	$m = 49.83$ $a = 50.17$ $b = 100$	$m = -50.38$ $a = 49.62$ $b = 80$
$\log_{10}(\beta)$	$\log_{10}(\text{km}^{-1})$	beta	$m = 44.76$ $a = 48.25$ $b = 50$	$m = -52.72$ $a = 47.28$ $b = 70$
Z/β	$\log_{10}(\text{cm}^2)$	beta	$m = -54.33$ $a = 45.68$ $b = 35$	$m = 39.55$ $a = 46.52$ $b = 57.7$

If v_D is small (very negative), then it belongs to the fuzzy set precipitation. If v_D is large, then it belongs to the fuzzy set cloud. What constitutes "large" and "small," and the resulting levels of membership of v_D in both the cloud and the precipitation sets, is determined mathematically by membership functions reported in Table 1.

For a hydrometeor-filled volume of air, inference of the membership of the entire set of accompanying remote sensing observations within both the cloud and the precipitation sets are accomplished via the "Mamdani implication" (Mendel 2001): the product of the memberships of all remote sensing observations in the cloud set is taken and likewise for their memberships in the precipitation set. Then, if the total product of memberships in the cloud fuzzy set is greater than in the precipitation fuzzy set, the "maximum defuzzifier" (Mendel 2001) classifies the volume as cloudy (and vice versa).

Data used to develop the membership functions were taken entirely from CSET below cloud-level legs. Those measurements used to this end are HCR mean Doppler velocity, HSRL backscatter, and reflectivity-to-backscatter ratio (Table A1). Single cloud-layer, zenith-dwelling scenes where cloud base is well determined using the HSRL and where it is plainly seen from the HCR that there is only one cloud layer were handpicked from the entire CSET campaign.

Once the scenes were chosen, remote sensing measurements were segregated and aggregated by whether they were observed above or below cloud base. Observations from above cloud base were associated with the fuzzy set cloud, and those observed below cloud base were associated with the fuzzy set precipitation. The statistics of these two aggregations of measurements were used to construct the membership functions for the cloud and precipitation fuzzy logic sets. The empirical membership functions are parameterized using beta functions [Liu and Chandrasekar 2000; Eq. (A1)]:

$$f(x; m, a, b) = \frac{1}{\left[1 + \left(\dfrac{x - m}{a}\right)^2\right]^b}. \tag{A1}$$

REFERENCES

Abel, S. J., and Coauthors, 2017: The role of precipitation in controlling the transition from stratocumulus to cumulus clouds in a Northern Hemisphere cold-air outbreak. *J. Atmos. Sci.*, **74**, 2293–2314, https://doi.org/10.1175/JAS-D-16-0362.1.

Albrecht, B., M. Fang, and V. Ghate, 2016: Exploring stratocumulus cloud-top entrainment processes and parameterizations by using Doppler cloud radar observations. *J. Atmos. Sci.*, **73**, 729–742, https://doi.org/10.1175/JAS-D-15-0147.1.

——, and Coauthors, 2019: Cloud System Evolution in the Trades (CSET): Following the evolution of boundary layer cloud systems with the NSF–NCAR GV. *Bull. Amer. Meteor. Soc.*, **100**, 93–121, https://doi.org/10.1175/BAMS-D-17-0180.1.

Biter, C. J., J. E. Dye, D. Huffman, and W. D. King, 1987: The dropsize response of the CSIRO liquid water probe. *J. Atmos. Oceanic Technol.*, **4**, 359–367, https://doi.org/10.1175/1520-0426(1987)004<0359:TDSROT>2.0.CO;2.

Bony, S., and J. L. Dufresne, 2005: Marine boundary layer clouds at the heart of tropical cloud feedback uncertainties in climate models. *Geophys. Res. Lett.*, **32**, L20806, https://doi.org/10.1029/2005GL023851.

Borque, P., E. Luke, and P. Kollias, 2016: On the unified estimation of turbulence eddy dissipation rate using Doppler cloud radars and lidars. *J. Geophys. Res. Atmos.*, **121**, 5972–5989, https://doi.org/10.1002/2015JD024543.

Bretherton, C. S., and M. C. Wyant, 1997: Moisture transport, lower-tropospheric stability, and decoupling of cloud-topped boundary layers. *J. Atmos. Sci.*, **54**, 148–167, https://doi.org/10.1175/1520-0469(1997)054<0148:MTLTSA>2.0.CO;2.

——, and Coauthors, 2019: Cloud, aerosol, and boundary layer structure across the northeast Pacific stratocumulus–cumulus transition as observed during CSET. *Mon. Wea. Rev.*, https://doi.org/10.1175/MWR-D-18-0281.1, in press.

Chen, M.-Y., and Y.-H. Chu, 2011: Beam broadening effect on Doppler spectral width of wind profiler. *Radio Sci.*, **46**, RS5013, https://doi.org/10.1029/2011RS004704.

Chu, Y., 2002: Beam broadening effect on oblique MST radar Doppler spectrum. *J. Atmos. Oceanic Technol.*, **19**, 1955–1967, https://doi.org/10.1175/1520-0426(2002)019<1955:BBEOOM>2.0.CO;2.

Clothiaux, E. E., T. P. Ackerman, and D. M. Babb, 1996: Ground-based remote sensing of cloud properties using millimeter-wave radar. *Radiation and Water in the Climate System*, E. Raschke, Ed., NATO ASI Series, Vol. 45, Springer, 323–366.

——, ——, G. G. Mace, K. P. Moran, R. T. Marchand, M. A. Miller, and B. E. Martner, 2000: Objective determination of cloud heights and radar reflectivities using a combination of active remote sensors at the ARM CART sites. *J. Appl. Meteor.*, **39**, 645–665, https://doi.org/10.1175/1520-0450(2000)039<0645:ODOCHA>2.0.CO;2.

Comstock, K., S. E. Yuter, R. Wood, and C. S. Bretherton, 2007: The three-dimensional structure and kinematics of drizzling stratocumulus. *Mon. Wea. Rev.*, **135**, 3767–3784, https://doi.org/10.1175/2007MWR1944.1.

Dong, X., and G. G. Mace, 2003: Profiles of low-level stratus cloud microphysics deduced from ground-based measurements.

J. Atmos. Oceanic Technol., **20**, 42–53, https://doi.org/10.1175/1520-0426(2003)020<0042:POLLSC>2.0.CO;2.

Eloranta, E., 2005: High spectral resolution lidar. *Lidar: Range-Resolved Optical Remote Sensing of the Atmosphere*, C. Weitkamp, Ed., Springer Series in Optical Sciences, Springer-Verlag, 143–163.

Fang, M., B. A. Albrecht, V. P. Ghate, and P. Kollias, 2014: Turbulence in continental stratocumulus, part I: External forcings and turbulence structures. *Bound.-Layer Meteor.*, **150**, 341–360, https://doi.org/10.1007/s10546-013-9873-3.

——, ——, E. Jung, P. Kollias, H. Jonsson, and I. PopStefanija, 2017: Retrieval of vertical air motion in precipitating clouds using Mie scattering and comparison with in situ measurements. *J. Appl. Meteor. Climatol.*, **56**, 537–553, https://doi.org/10.1175/JAMC-D-16-0158.1.

Feng, Z., S. A. McFarlane, C. Schumacher, S. Ellis, J. Comstock, and N. Bharadwaj, 2014: Constructing a merged cloud–precipitation radar dataset for tropical convective clouds during the DYNAMO/AMIE experiment at Addu Atoll. *J. Atmos. Oceanic Technol.*, **31**, 1021–1042, https://doi.org/10.1175/JTECH-D-13-00132.1.

Fielding, M. D., J. C. Chiu, R. J. Hogan, G. Feingold, E. Eloranta, E. J. O'Connor, and M. P. Cadeddu, 2015: Joint retrievals of cloud and drizzle in marine boundary layer clouds using ground-based radar, lidar and zenith radiances. *Atmos. Meas. Tech.*, **8**, 2663–2683, https://doi.org/10.5194/amt-8-2663-2015.

Frisch, A. S., C. W. Fairall, and J. B. Snider, 1995: Measurement of stratus cloud and drizzle parameters in ASTEX with a K_α-band Doppler radar and a microwave radiometer. *J. Atmos. Sci.*, **52**, 2788–2799, https://doi.org/10.1175/1520-0469(1995)052<2788:MOSCAD>2.0.CO;2.

Frisch, S., M. Shupe, I. Djalalova, G. Feingold, and M. Poellot, 2002: The retrieval of stratus cloud droplet effective radius with cloud radars. *J. Atmos. Oceanic Technol.*, **19**, 835–842, https://doi.org/10.1175/1520-0426(2002)019<0835:TROSCD>2.0.CO;2.

Ghate, V. P., B. A. Albrecht, and P. Kollias, 2010: Vertical velocity structure of nonprecipitating continental boundary layer stratocumulus clouds. *J. Geophys. Res.*, **115**, D13204, https://doi.org/10.1029/2009JD013091.

——, M. A. Miller, and L. DiPretore, 2011: Vertical velocity structure of marine boundary layer trade wind cumulus clouds. *J. Geophys. Res.*, **116**, D16206, https://doi.org/10.1029/2010JD015344.

——, M. C. Schwartz, J. Vivekanandan, and E. Eloranta, 2016: Hydrometeor mask and cloud boundaries data, version 1.0. UCAR/NCAR Earth Observing Laboratory, accessed 21 April 2018, https://doi.org/10.5065/D63T9FM0.

Giangrande, S. E., E. P. Luke, and P. Kollias, 2010: Automated retrievals of precipitation parameters using non-Rayleigh scattering at 95 GHz. *J. Atmos. Oceanic Technol.*, **27**, 1490–1503, https://doi.org/10.1175/2010JTECHA1343.1.

Gossard, E. E., R. O. Strauch, and R. R. Rogers, 1990: Evolution of dropsize distributions in liquid precipitation observed by ground-based Doppler radar. *J. Atmos. Oceanic Technol.*, **7**, 815–828, https://doi.org/10.1175/1520-0426(1990)007<0815:EODDIL>2.0.CO;2.

Hildebrand, P. H., and R. S. Sekhon, 1974: Objective determination of the noise level in Doppler spectra. *J. Appl. Meteor.*, **13**, 808–811, https://doi.org/10.1175/1520-0450(1974)013<0808:ODOTNL>2.0.CO;2.

Illingworth, A. J., and Coauthors, 2007: Cloudnet: Continuous evaluation of cloud profiles in seven operational models using ground-based observations. *Bull. Amer. Meteor. Soc.*, **88**, 883–898, https://doi.org/10.1175/BAMS-88-6-883.

Klingebiel, M., and Coauthors, 2015: Arctic low-level boundary layer clouds: In situ measurements and simulations of mono- and bimodal supercooled droplet size distributions at the top layer of the liquid phase clouds. *Atmos. Chem. Phys.*, **15**, 617–631, https://doi.org/10.5194/acp-15-617-2015.

Kollias, P., B. A. Albrecht, and F. Marks, 2002: Why Mie? *Bull. Amer. Meteor. Soc.*, **83**, 1471–1484, https://doi.org/10.1175/BAMS-83-10-1471.

——, J. Rémillard, E. Luke, and W. Szyrmer, 2011: Cloud radar Doppler spectra in drizzling stratiform clouds: 1. Forward modeling and remote sensing applications. *J. Geophys. Res.*, **116**, D13201, https://doi.org/10.1029/2010JD015237.

——, N. Bharadwaj, K. Widener, I. Jo, and K. Johnson, 2014: Scanning ARM cloud radars. Part I: Operational sampling strategies. *J. Atmos. Oceanic Technol.*, **31**, 569–582, https://doi.org/10.1175/JTECH-D-13-00044.1.

Kotthaus, S., E. O'Connor, C. Münkel, C. Charlton-Perez, M. Haeffelin, A. M. Gabey, and C. S. B. Grimmond, 2016: Recommendations for processing atmospheric attenuated backscatter profiles from Vaisala CL31 ceilometers. *Atmos. Meas. Tech.*, **9**, 3769–3791, https://doi.org/10.5194/amt-9-3769-2016.

Kovalev, V. A., and W. E. Eichinger, 2004: *Elastic Lidar: Theory, Practice, and Analysis Methods.* John Wiley and Sons, 619 pp.

Lareau, N. P., Y. Zhang, and S. A. Klein, 2018: Observed boundary layer controls on shallow cumulus at the ARM Southern Great Plains site. *J. Atmos. Sci.*, **75**, 2235–2255, https://doi.org/10.1175/JAS-D-17-0244.1.

Laursen, K., D. Jorgensen, G. Brasseur, S. Ustin, and J. Huning, 2006: HIAPER: The next generation NSF/NCAR research aircraft. *Bull. Amer. Meteor. Soc.*, **87**, 896–909, https://doi.org/10.1175/BAMS-87-7-896.

Liu, H., and V. Chandrasekar, 2000: Classification of hydrometeors based on polarimetric radar measurements: Development of fuzzy logic and neuro-fuzzy systems, and in situ verification. *J. Atmos. Oceanic Technol.*, **17**, 140–164, https://doi.org/10.1175/1520-0426(2000)017<0140:COHBOP>2.0.CO;2.

Luke, E. P., and P. Kollias, 2013: Separating cloud and drizzle radar moments during precipitation onset using Doppler spectra. *J. Atmos. Oceanic Technol.*, **30**, 1656–1671, https://doi.org/10.1175/JTECH-D-11-00195.1.

Mather, J. H., and J. W. Voyles, 2013: The ARM Climate Research Facility: A review of structure and capabilities. *Bull. Amer. Meteor. Soc.*, **94**, 377–392, https://doi.org/10.1175/BAMS-D-11-00218.1.

McGill, M., and Coauthors, 2004: Combined lidar-radar remote sensing: Initial results from CRYSTAL-FACE. *J. Geophys. Res.*, **109**, D07203, https://doi.org/10.1029/2003JD004030.

Mendel, J. M., 2001: *Uncertain Rule-Based Fuzzy Logic Systems: Introduction and New Directions.* Prentice Hall, 555 pp.

Miles, N. L., J. Verlinde, and E. E. Clothiaux, 2000: Cloud droplet size distributions in low-level stratiform clouds. *J. Atmos. Sci.*, **57**, 295–311, https://doi.org/10.1175/1520-0469(2000)057<0295:CDSDIL>2.0.CO;2.

Miller, K. S., and M. M. Rochwarger, 1972: A covariance approach to spectral moment estimation. *IEEE Trans. Inf. Theory*, **18**, 588–596, https://doi.org/10.1109/TIT.1972.1054886.

O'Connor, E. J., R. J. Hogan, and A. J. Illingworth, 2005: Retrieving stratocumulus drizzle parameters using Doppler radar and lidar. *J. Appl. Meteor.*, **44**, 14–27, https://doi.org/10.1175/JAM-2181.1.

Painemal, D., and P. Zuidema, 2013: The first aerosol indirect effect quantified through airborne remote sensing during VOCALS-REx. *Atmos. Chem. Phys.*, **13**, 917–931, https://doi.org/10.5194/acp-13-917-2013.

Pazmany, A., 2007: A compact 183 GHz radiometer for airborne and ground-based water vapor and liquid water sensing. *IEEE Trans. Geosci. Remote Sens.*, **45**, 2202–2206, https://doi.org/10.1109/TGRS.2006.888104.

Rauber, R. M., S. M. Ellis, J. Vivekanandan, J. Stith, W. Lee, G. M. McFarquhar, B. F. Jewett, and A. Janiszeski, 2017: Finescale structure of a snowstorm over the northeastern United States: A first look at high-resolution HIAPER cloud radar observations. *Bull. Amer. Meteor. Soc.*, **98**, 253–269, https://doi.org/10.1175/BAMS-D-15-00180.1.

Rilling, R., U. Romatschke, J. Vivekanandan, and S. M. Ellis, 2017: A proxy calibration monitoring technique for the NCAR airborne W-band radar. *General Assembly 2017*, Vienna, Austria, European Geosciences Union, X4.185.

Sandu, I., and B. Stevens, 2011: On the factors modulating the stratocumulus to cumulus transitions. *J. Atmos. Sci.*, **68**, 1865–1881, https://doi.org/10.1175/2011JAS3614.1.

——, ——, and R. Pincus, 2010: On the transitions in marine boundary layer cloudiness. *Atmos. Chem. Phys.*, **10**, 2377–2391, https://doi.org/10.5194/acp-10-2377-2010.

Sloss, P. W., and D. Atlas, 1968: Wind shear and reflectivity gradient effects on Doppler radar spectra. *J. Atmos. Sci.*, **25**, 1080–1089, https://doi.org/10.1175/1520-0469(1968)025<1080:WSARGE>2.0.CO;2.

Smith, P. L., 1982: On the graphical presentations of raindrop size data. *Atmos.–Ocean*, **20**, 4–16, https://doi.org/10.1080/07055900.1982.9649124.

Stein, A. F., R. R. Draxler, G. D. Rolph, B. J. Stunder, M. D. Cohen, and F. Ngan, 2015: NOAA's HYSPLIT atmospheric transport and dispersion modeling system. *Bull. Amer. Meteor. Soc.*, **96**, 2059–2077, https://doi.org/10.1175/BAMS-D-14-00110.1.

Stephens, G. L., 2005: Cloud feedbacks in the climate system: A critical review. *J. Climate*, **18**, 237–273, https://doi.org/10.1175/JCLI-3243.1.

Terai, C., R. Wood, C. Leon, and P. Zuidema, 2012: Does precipitation susceptibility vary with increasing cloud thickness in marine stratocumulus? *Atmos. Chem. Phys.*, **12**, 4567–4583, https://doi.org/10.5194/acp-12-4567-2012.

Testud, J., S. Oury, R. A. Black, P. Amayenc, and X. Dou, 2001: The concept of "normalized" distribution to describe raindrop spectra: A tool for cloud physics and cloud remote sensing. *J. Appl. Meteor.*, **40**, 1118–1140, https://doi.org/10.1175/1520-0450(2001)040<1118:TCONDT>2.0.CO;2.

Tiedtke, M., 1993: Representation of clouds in large-scale models. *Mon. Wea. Rev.*, **121**, 3040–3061, https://doi.org/10.1175/1520-0493(1993)121<3040:ROCILS>2.0.CO;2.

Vivekanandan, J., D. S. Zrnic, S. M. Ellis, R. Oye, A. V. Ryzhkov, and J. Straka, 1999: Cloud microphysics retrieval using S-band dual-polarization radar measurements. *Bull. Amer. Meteor. Soc.*, **80**, 381–388, https://doi.org/10.1175/1520-0477(1999)080<0381:CMRUSB>2.0.CO;2.

——, and Coauthors, 2015: A wing pod-based millimeter wavelength airborne cloud radar. *Geosci. Instrum. Methods Data Syst.*, **4**, 161–176, https://doi.org/10.5194/gi-4-161-2015.

Wang, S., B. Albrecht, and P. Minnis, 1993: A regional simulation of marine boundary-layer clouds. *J. Atmos. Sci.*, **50**, 4022–4043, https://doi.org/10.1175/1520-0469(1993)050<4022:ARSOMB>2.0.CO;2.

Wang, Z., P. Wechsler, W. Kuestner, J. French, A. Rodi, B. Glover, M. Burkhart, and D. Lukens, 2009: Wyoming cloud lidar: Instrument description and applications. *Opt. Express*, **17**, 13 576–13 587, https://doi.org/10.1364/OE.17.013576.

——, and Coauthors, 2012: Single aircraft integration of remote sensing and in situ sampling for the study of cloud microphysics and dynamics. *Bull. Amer. Meteor. Soc.*, **93**, 653–668, https://doi.org/10.1175/BAMS-D-11-00044.1.

Wetherald, R. T., and S. Manabe, 1988: Cloud feedback processes in a general circulation model. *J. Atmos. Sci.*, **45**, 1397–1415, https://doi.org/10.1175/1520-0469(1988)045<1397:CFPIAG>2.0.CO;2.

Wiscombe, W. J., 1980: Improved Mie scattering algorithms. *Appl. Opt.*, **19**, 1505–1509, https://doi.org/10.1364/AO.19.001505.

Wood, R., 2012: Stratocumulus clouds. *Mon. Wea. Rev.*, **140**, 2373–2423, https://doi.org/10.1175/MWR-D-11-00121.1.

——, and C. S. Bretherton, 2004: Boundary layer depth, entrainment, and decoupling in the cloud-capped subtropical and tropical marine boundary layer. *J. Climate*, **17**, 3576–3588, https://doi.org/10.1175/1520-0442(2004)017<3576:BLDEAD>2.0.CO;2.

——, and D. L. Hartmann, 2006: Spatial variability of liquid water path in marine low cloud: The importance of mesoscale cellular convection. *J. Climate*, **19**, 1748–1764, https://doi.org/10.1175/JCLI3702.1.

——, D. Leon, M. Lebsock, J. Snider, and A. D. Clarke, 2012: Precipitation driving of droplet concentration variability in marine low clouds. *J. Geophys. Res.*, **117**, D19210, https://doi.org/10.1029/2012JD018305.

——, and Coauthors, 2018: Ultraclean layers and optically thin clouds in the stratocumulus to cumulus transition. Part I: Observations. *J. Atmos. Sci.*, **75**, 1631–1652, https://doi.org/10.1175/JAS-D-17-0213.1.

Yamaguchi, T., G. Feingold, and J. Kazil, 2017: Stratocumulus to cumulus transition by drizzle. *J. Adv. Model. Earth Syst.*, **9**, 2333–2349, https://doi.org/10.1002/2017MS001104.

Yuter, S. E., and R. A. Houze Jr., 1995: Three-dimensional kinematic and microphysical evolution of Florida cumulonimbus. Part II: Frequency distribution of vertical velocity, reflectivity, and differential reflectivity. *Mon. Wea. Rev.*, **123**, 1941–1963, https://doi.org/10.1175/1520-0493(1995)123<1941:TDKAME>2.0.CO;2.

Zhang, M., and Coauthors, 2013: CGILS: Results from the first phase of an international project to understand the physical mechanisms of low cloud feedbacks in single column models. *J. Adv. Model. Earth Syst.*, **5**, 826–842, https://doi.org/10.1002/2013MS000246.

Zrnic, D. S., 1977: Spectral moment estimates from correlated pulse pairs. *IEEE Trans. Aerosp. Electron. Syst.*, **13**, 344–345, https://doi.org/10.1109/TAES.1977.308467.

Zuidema, P., D. Leon, A. Pazmany, and M. Cadeddu, 2012: Aircraft millimeter-wave passive sensing of cloud liquid water and water vapor during VOCALS-REx. *Atmos. Chem. Phys.*, **12**, 355–369, https://doi.org/10.5194/acp-12-355-2012.